PAPER

Check for updates

Synthesis of SrTiO$_3$ and Al-doped SrTiO$_3$ *via* the deep eutectic solvent route†

Adedoyin N. Adeyemi, [ID] [a] Amrit Venkatesh, [ID] [ab] Chengcan Xiao, [c] Zeqiong Zhao, [c] Ying Li, [ID] [a] Tori Cox, [a] Dapeng Jing, [ID] [bd] Aaron J. Rossini, [ID] [ab] Frank E. Osterloh [ID] [c] and Julia V. Zaikina [ID] *[a]

SrTiO$_3$ and aluminum-doped SrTiO$_3$ are synthesized by calcination of metal salts dissolved in a deep eutectic solvent (DES) without any post-synthesis treatment. The DES used is the eutectic mixture of choline chloride (hydrogen bond acceptor) and malonic acid (hydrogen bond donor). Titanium(IV) oxide bis(2,4-pentanedionate) is utilized as the non-volatile, easy-to-handle, DES-soluble titanium precursor. The ammonia gas evolved during the calcination process provides a reducing atmosphere, resulting in the formation of Ti^{3+} and oxygen vacancies within the SrTiO$_3$ matrix. According to UV-Vis spectroscopy and X-ray photoelectron spectroscopy, the amount of Ti^{3+} species and oxygen vacancies (V$_O$) in the synthesized perovskite can be tuned by varying the duration of the calcination process and by adding Al^{3+} dopants. Solid state ^{27}Al NMR spectroscopy and powder X-ray diffraction confirm the doping of aluminum into the octahedral site of the perovskite structure. Surface photovoltage spectroscopy confirms that Al^{3+} dopants can eliminate Ti^{3+} defects in Al-doped SrTiO$_3$. Ultraviolet illumination experiments in water and aqueous methanol show that SrTiO$_3$ and aluminum-doped SrTiO$_3$, after modification with Rh$_x$Cr$_{2-x}$O$_3$ or Pt co-catalysts, evolve small amounts of H$_2$ (EQE of 0.0113–0.0173% at 375 nm) with only traces of O$_2$ detected. The lack of photocatalytic activity is attributed to rapid electron-hole recombination in the oxygen vacancy-rich materials and to the lack of crystal facets that could aid charge separation.

[a] Department of Chemistry, Iowa State University, Ames, Iowa 50011, USA.
 E-mail: yzaikina@iastate.edu
[b] Ames Laboratory, US DOE, Iowa State University, Ames, Iowa 50011, USA
[c] Department of Chemistry, University of California at Davis, Davis, California
 95616, USA
[d] Materials Analysis and Research Laboratory, Iowa State University, Ames,
 IA 50011, USA
† Electronic supplementary information (ESI) available. See DOI: https://doi.org/
10.1039/d2ma00404f

Introduction

Deep eutectic solvents (DESs) are analogs of ionic liquids (ILs).[1–3] Unlike conventional ILs, which are made up of discrete ions, DESs are made of a hydrogen bond acceptor (usually quaternary ammonium halides) and a hydrogen bond donor, thus DESs possess both hydrogen bonding and ionic interactions. The majority of DESs utilize 2-hydroxyethyltrimethylammonium chloride (choline chloride) as the hydrogen bond acceptor combined with a hydrogen bond donor such as urea, oxalic acid, citric acid, or acetamide, *etc.*[2,4] When these two solids are mixed, they form a low melting eutectic mixture, that is a liquid at room temperature.[1] DESs are non-toxic and biodegradable solvents; they have low melting points and are environmentally friendly.[5] Owing to the high solubility of selected

binary oxide or metal precursors in DESs,[3] they are attractive replacements for corrosive inorganic acids as a reaction medium in solution synthesis of materials.[3] Several ternary oxides such as spinel-type ferrite nanoparticles,[6] zinc and copper vanadates like M$_2$V$_2$O$_7$ and MV$_2$O$_6$ (M = Zn or Cu),[7,8] and barium titanate BaTiO$_3$[9] have been previously synthesized using the DES route. Except for BaTiO$_3$, these ternary oxides were synthesized by dissolving binary metal oxides in DESs, followed by calcination of the resulting solution in air at 500 °C or higher temperatures. BaTiO$_3$ was synthesized from barium acetate and titanium isopropoxide,[9] because unlike many other binary oxides, TiO$_2$ is insoluble in any of the studied DESs.[3]

Strontium titanate, SrTiO$_3$ is a functional oxide often used as a dielectric material[10–12] and has been recently investigated for thermoelectric applications.[13,14] It is also a semiconductor with reported bandgaps in the range of 3.0 eV to 3.88 eV.[15–18] Due to the size of the band gap and the position of the valence/conduction band edge, strontium titanate, is a suitable catalyst for overall photocatalytic water splitting.[19,20]

SrTiO$_3$ exists as an intrinsic non-stoichiometric compound which contains two types of defects: oxygen vacancies and Ti^{3+} species. When the Ti–O bond breaks, O$_2$ gas is released to yield oxygen vacancies as well as free electrons, which reduce Ti^{4+}

to Ti^{3+}. The doping of $SrTiO_3$ with aliovalent metal cations, specifically a lower valence cation in either of the cation sites (*i.e.* doping Sr^{2+} site with a +1 cation or doping Ti^{4+} site with a +3 cation) can be used to enhance its photocatalytic activity by suppressing the formation of Ti^{3+}, which acts as an electron-hole recombination center.[21,22] For example, a strong increase in water splitting activity was observed by doping Al^{3+} into $SrTiO_3$ *via* solid-state synthesis.[22–25]

$SrTiO_3$ has been made *via* several synthetic routes such as solid-state,[26–29] sol–gel,[30–33] and hydrothermal synthetic methods.[34–36] Like with most functional compounds, properties of $SrTiO_3$ can be tuned *via* different synthetic routes that impact the dopant fraction, crystallinity, crystallite size and morphology. Typically, when reactants are liquids or in solution, this leads to a faster reaction because of the enhanced diffusion.

Here we report the synthesis and characterization of $SrTiO_3$ and Al-doped $SrTiO_3$ made through the environmentally benign choline chloride–malonic acid DES route without any post-synthesis treatment. Unlike previously reported synthesis of titanates, we utilized titanium(IV) oxide bis(2,4-pentanedionate) as a convenient and non-volatile Ti-precursor, which is easily dissolved in the employed DES. Two different heating profiles were employed to obtain $SrTiO_3$ and Al-doped $SrTiO_3$ with different properties. Furthermore, the site to which aluminum is being doped was investigated using ^{27}Al solid-state nuclear magnetic resonance (NMR) spectroscopy. Lastly, the ability of the synthesized materials to function as photocatalysts for the overall water splitting reaction was studied.

Experimental

Materials and methods

Malonic acid $CH_2(COOH)_2$ (Alfa Aesar, 99%, crystalline), strontium nitrate $Sr(NO_3)_2$ (Alfa Aesar, 99.9%), titanium(IV) oxide bis(2,4-pentanedionate) $(CH_3COCHCOCH_3)_2TiO$ (TOPD) (Alfa Aesar, 99.9%), and aluminum 2,4-pentanedionate $(CH_3COCHCOCH_3)_3Al$ (AlPD) (Alfa Aesar, 99.6% min) were used as received without any further purification. Choline chloride $(CH_3)_3N(Cl)CH_2CH_2OH$ (Sigma-Aldrich, 98%) was dried at 120 °C for 10 hours under vacuum prior to use. Fluorine-doped tin oxide (FTO) substrates (MTI corporation) were washed with detergent and deionized water, followed by 15 minutes of sonication in acetone, ethanol and ultra-purified water in series and drying in a 70 °C oven in air overnight.

The deep eutectic solvent (DES) was prepared by mixing malonic acid and choline chloride (1:1 molar ratio) in a parafilm-covered glass beaker at 85 °C while stirring, until a clear viscous liquid DES was obtained.

In a typical synthesis of $SrTiO_3$, 0.47 mmol (0.0995 g) of $Sr(NO_3)_2$ was dissolved in 35.904 g of DES (density of DES is 1.21 g mL^{-1}) to make a 0.16 M solution, while 0.47 mmol (0.123 g) of TOPD was dissolved in 126.6 g of DES to make 0.0045 M solution. These two solutions were made in separate beakers until a clear solution was obtained in both cases. The

resulting solutions were further mixed under vigorous stirring for 3 to 5 hours in a parafilm-covered beaker. About 7 g of the resulting solution was transferred to a 50 mL porcelain crucible and calcined in a Thermolyne Thermofisher muffle furnace. Two different heating profiles were used for sample syntheses.

Heating profile 1. The solution containing the dissolved precursor was heated to 230 °C at the rate of 2 °C min^{-1} and left at this temperature for 6 hours, then heated to 500 °C at the rate of 2 °C min^{-1} for 6 hours, and finally heated to 950 °C at the rate of 10 °C min^{-1}, left at that temperature for 6 hours and cooled to room temperature by switching off the furnace. The product yield (based on moles of $Sr(NO_3)_2$) using this heating profile is about 77%.

Heating profile 2. The solution containing the dissolved precursor was heated to 500 °C at the rate of about 23 °C min^{-1} (fastest rate for this type of furnace), dwelled at 500 °C for 6 hours, then heated to 950 °C at the rate of 10 °C min^{-1}, left at that temperature for 1 hour and naturally cooled to room temperature by switching off the furnace. The product yield (based on moles of $Sr(NO_3)_2$) using this heating profile is about 23%.

Al-Doped $SrTiO_3$, *e.g.* $SrTi_xAl_{(1−x)}O_3$, x = 0, 0.025, 0.05, 0.1, 0.2, was made using heating profile 1 and 2 by similar synthesis procedures as $SrTiO_3$. In a typical synthesis of $SrTi_{0.9}Al_{0.1}O_3$, three separate solutions were prepared: (1) 0.47 mmol (0.0995 g) of $Sr(NO_3)_2$ was dissolved in 35.904 g of DES; (2) 0.423 mmol (0.111 g) of TOPD was dissolved in 113.5 g of DES to make 0.0045 M solution; (3) 0.047 mmol (0.0152 g) of AlPD was dissolved in 12.2 g of DES to make 0.0045 M solution of AlPD in DES. The three solutions were then mixed and calcined as previously described for $SrTiO_3$.

Characterization

Powder X-ray diffraction. Samples were characterized by powder X-ray diffraction (PXRD) using a Rigaku Miniflex 600 diffractometer with Cu Kα X-ray radiation (λ = 1.54051 Å). Data were collected using a zero-background holder at room temperature in air. Phase identification was performed using the PDF-2 database with PDXL software.[37] The determination of unit cells of doped and undoped samples was done by mixing the synthesized samples with an internal standard such as LaB_6 ($Pm\bar{3}m$, a = 4.1566 Å). The data was analyzed by the Rietveld refinement method using Jana2006 software package.[38]

Diffuse reflectance UV-Vis spectroscopy. Diffuse reflectance UV-Vis spectra were collected using a BLACK-Comet C-SR-100 spectrometer with SL1 Tungsten Halogen lamp as source of vis-IR radiation and SL3 Deuterium Lamp as source of UV radiation. Compacted samples were prepared on glass slides by flattening the solids with a metal spatula. Direct and indirect bandgap values for samples were estimated by extrapolating the linear slope of Tauc plots.

X-Ray photoelectron spectroscopy (XPS). The XPS measurements were performed on a Kratos Amicus/ESCA 3400 instrument. The samples were irradiated with 240 W non-monochromated Mg Kα X-rays as an irradiation source. Photoelectrons emitted at 0° from the surface normal with the pass

energy of 150 eV were energy analysed using a DuPont analyser. Raw data files were processed using CasaXPS, and a Shirley baseline was applied to all spectra.

Scanning electron microscopy (SEM) and energy dispersive X-ray spectroscopy (EDXS). The morphology of the synthesized samples was inspected using SEM utilizing an FEI Quanta 250 field emission scanning electron microscope at 15 kV. EDXS was performed using Oxfords X-Max 80 detector for elemental composition analysis. Powdered samples were deposited on a SEM sample holder using carbon tape. The samples were coated with 5 nm of iridium metal.

Solid-state NMR spectroscopy. ^{27}Al solid-state NMR was carried out on all the samples using a Bruker widebore 9.4 T (400 MHz) NMR spectrometer equipped with an Avance III HD console. Spectra were acquired using a 2.5 mm triple-resonance (HXY) MAS probe. The MAS rate was 25 kHz in all cases. A standard pulse-acquire method with a ^{27}Al pulse duration of 0.3 μs corresponding to an 8° tip angle (ca. 75 kHz rf field) was used to obtain quantitative ^{27}Al solid-state NMR spectra.[39,40] Spectra were processed using the Bruker Topspin package; deconvolution of the different ^{27}Al signals and fitting to Czjzek distribution[41] was performed using the ssNake program.[42]

Surface photovoltage (SPV) spectroscopy. SPV spectroscopy was performed on particle films on fluorine-doped tin oxide (FTO) substrates. These films were prepared by drop coating aqueous SrTiO$_3$ and Al-doped SrTiO$_3$ suspensions (5 mg mL^{-1}) onto the FTO, followed by annealing at 300 °C for 2 h in air. SPV measurements were done under vacuum (1×10^{-4} mbar) with a vibrating gold mesh Kelvin probe (Besocke Delta phi). Monochromatic light used as the irradiation source was produced by a 150 W Xe lamp and an Oriel Cornerstone 130 monochromator. The light intensity at the sample surface is 1–3 mW cm^{-2}. Spectra were acquired by stepping the photon energy by 0.0124 eV every 5 s and by measuring the contact potential difference (CPD) value at each step. All CPD values in Fig. 11 are reported relative to the CPD value in the dark. Positive values correspond to electrons moving toward the Kelvin probe and negative values correspond to electrons moving away from the Kelvin probe. Additional details can be found elsewhere.[43]

Deposition of the cocatalysts. Rh$_x$Cr$_{2−x}$O$_3$ cocatalyst was loaded onto the surface of SrTiO$_3$ or SrTiO$_3$:Al particles with a weight ratio of Rh:Cr:SrTiO$_3$ (or SrTiO$_3$:Al) = 1:1:1000, as described previously.[44] Typically, 150 mg SrTiO$_3$ or SrTiO$_3$:Al was mixed with appropriate amount of RhCl$_3$ and Cr(NO$_3$)$_3$ solutions containing 0.15 mg Rh and 0.15 mg Cr in a vial in a 70 °C water bath, and water was slowly evaporated under constant stirring. The product was then transferred to a furnace and heated at 350 °C in air for 1 h to produce Rh$_x$Cr$_{2−x}$O$_3$ loaded SrTiO$_3$ or SrTiO$_3$:Al in 95% yield. Pt-modified SrTiO$_3$ and SrTi$_{0.9}$Al$_{0.1}$O$_3$ (heating profile 1) were made by photo-deposition, using 100 mg SrTiO$_3$ (SrTiO$_3$:Al) particles, a H$_2$PtCl$_6$ stock solution (2 mg Pt mL^{-1}) and 100 mL 20% of aqueous methanol solution with the weight percentage of Pt to SrTiO$_3$ (or SrTiO$_3$:Al) being 2%. The mixture was sonicated for 10 min and bubbled with N$_2$ for 10 min, then connected to the online Gas Chromatography system (SRI 8610c) with a 300W Xe

lamp and magnetic stirring. H$_2$ generation was recorded during photo-deposition to pinpoint the end point of this process. A typical photo-deposition lasts for 4–5 hours until the H$_2$ generation rate becomes constant. After photo-deposition, the Pt loaded particles were centrifuged and washed with water for 3 times, re-suspended in 20% volume ratio methanol and made ready for hydrogen evolution experiment.

Photocatalytic experiments. The water splitting experiments were conducted in a quartz round bottom flask with a mixture of 100 mg Rh$_x$Cr$_{2−x}$O$_3$/SrTiO$_3$ (or Rh$_x$Cr$_{2−x}$O$_3$/SrTiO$_3$:Al) powder and 100 mL ultra-purified water using Xe-lamp. The suspension was sonicated for 10 min and bubbled with N$_2$ for 10 min before irradiation to remove any residual O$_2$ dissolved in it. Then, the flask was connected to the online Gas Chromatography system (SRI 8610c) with a 300W Xe lamp and magnetic stirring. UV intensity was measured to be 100 mW cm^{-2} with a GaN photodetector (SEL 270) connected to an ILT1400 International Light photometer. Hydrogen evolution reaction/External quantum efficiency (EQE) measurements were conducted similarly, using a mixture of 100 mg Pt/SrTiO$_3$ or Pt/SrTiO$_3$:Al in 118 mL of 20% aqueous methanol solution. The quartz flask was covered with aluminum foil leaving only a 1.531 cm^2 window for incident light from the 375 nm LED. The LED light intensity was measured with a SEL623 Thermopile detector connected to an ILT1400 International Light photometer. Details of EQE calculation are given in the Supporting Information.

Results and discussion

The DES employed in this synthesis was choline chloride–malonic acid mixed in a 1:1 molar ratio. TiO$_2$ is not soluble in any studied DES, but titanium isopropoxide has previously been utilized for the synthesis of BaTiO$_3$ using a DES.[9] However, both titanium isopropoxide and titanium(IV) chloride are flammable fuming liquids which readily undergoes hydrolysis upon contact with humid air, making them unpleasant precursors to work with. Here we utilized titanium(IV) oxide bis(2,4-pentanedionate)(TOPD)[45] as a DES-soluble precursor. TOPD, which is the source of titanium in this synthesis dissolves in the choline chloride–malonic acid DES to give a yellow viscous solution in a parafilm covered beaker. When a laser beam (from a laser pointer) is passed through the yellow viscous solution (Fig. 1(a)), no Tyndall scattering was observed, confirming that that TOPD indeed formed a true solution in DES, not just a dispersion of colloidal particles. TOPD is a more convenient precursor to use since it is a powder (thus easy to weigh) and it does not produce fumes unlike other typically used Ti precursors.

The resulting yellow stable viscous solution was transferred into an open porcelain crucible and calcined in air, removing the organic solvent. The organic components are combusted below or at 500 °C. Ammonia, hydrogen chloride, carbon dioxide and water are evolved as gaseous by-products. Powder X-ray diffraction (PXRD) patterns were collected *ex situ* at

Fig. 1 (a) Synthetic route of strontium titanate SrTiO$_3$. Atom color coding used: Sr (green), Ti (blue), O (red); (b) molecular structure of titanium(IV) oxide bis(2,4-pentanedionate) (TOPD); (c) molecular structure of aluminum 2,4-pentanedionate.

different calcination temperatures to monitor the progress of the reaction (Fig. 2). During the calcination of the transparent, yellow viscous solution, the sample remains amorphous up to 300 °C.

The first set of peaks appearing at 400 °C correspond to two phases: strontium chloride dihydrate (SrCl$_2$·2H$_2$O) and anatase TiO$_2$. Peaks of cubic SrTiO$_3$ (perovskite structure, $Pm\bar{3}m$) begin to appear at 600 °C with SrCl$_2$·2H$_2$O and anatase TiO$_2$ still present. As the peaks of SrTiO$_3$ become more intense, the intensity of SrCl$_2$·2H$_2$O peaks decrease. At 950 °C the reaction is complete, and SrTiO$_3$ is the primary product with a minor impurity of both anatase and rutile TiO$_2$ (5 wt%), as determined by Rietveld refinement of PXRD data. Overall, SrCl$_2$·2H$_2$O and

Fig. 2 *Ex situ* powder X-ray diffraction patterns of the calcined sample for the synthesis of SrTiO$_3$ at various temperatures. TiO$_2$ impurity peaks are marked with asterisks (*).

TiO$_2$ formed first, and further reaction occurs upon an increase in temperature to yield SrTiO$_3$. The result of this stepwise calcination process differs from the previously reported synthesis of BaTiO$_3$,[9] since the Bragg's peaks corresponding to SrTiO$_3$ appeared as early as 600 °C whereas peaks corresponding to BaTiO$_3$ were not observed until 850 °C. Additionally, the DES-assisted synthesis of BaTiO$_3$ proceeds through a BaCl$_2$ intermediate while that of SrTiO$_3$ proceeds through a SrCl$_2$·2H$_2$O intermediate. We hypothesize that the difference in the type of the chloride intermediates arises because for BaTiO$_3$ synthesis, precursors were stirred in an open container at 90 °C until water evaporated. In contrast, our synthesis of SrTiO$_3$ used stirring in a parafilm covered beaker which discourages evaporation. Since the little amount of water present in the hygroscopic choline chloride is not allowed to evaporate during mixing, this water may lead to the formation of a hydrated chloride intermediate, SrCl$_2$·2H$_2$O.

Due to the small concentration of metal precursors in the DES, the yellow viscous solution is very dilute. Two heating profiles are employed for the calcination process: heating profile 1 and heating profile 2. Heating profile 2 is similar to that used in the synthesis of BaTiO$_3$,[9] it is a rapid calcination and had an overall shorter dwelling time (see experimental details). It was observed that the primary yield of SrTiO$_3$ made from both heating profiles is ∼91%. The secondary yield, however, is different for samples made *via* different heating profiles. The samples made using heating profile 1 have large clusters, and can be easily transferred from the crucibles, leading to a higher secondary yield of 77% (occasionally, the yield can be as high as 88%). However, samples made by heating profile 2 are mostly sintered to the crucibles. Also, the particles are smaller, unclustered, lightweight, and so are easily lost during the transfer from the crucibles. This leads to a lower secondary yield when heating profile 2 is employed (23%).

The weight percent of impurities present in the synthesized samples was evaluated by Rietveld refinement of PXRD data.
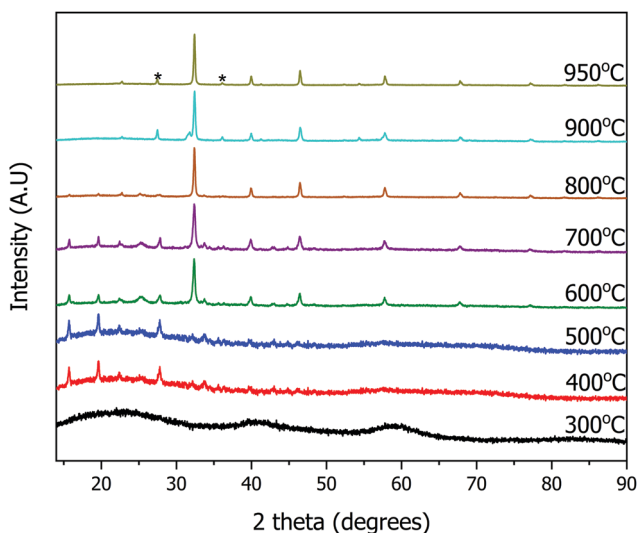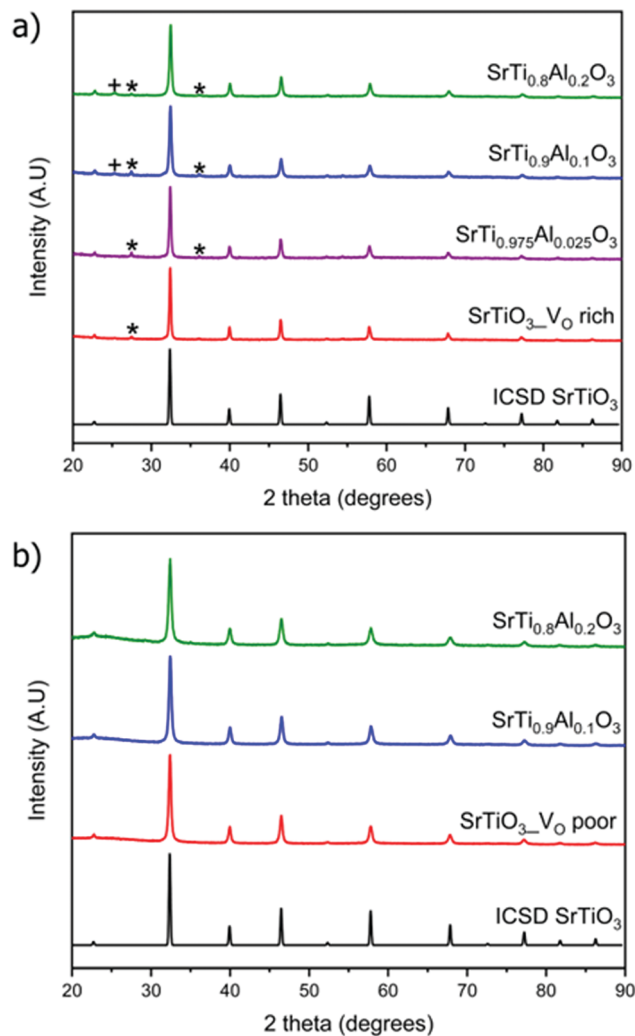
Fig. 3 Powder X-ray diffraction patterns of doped and undoped (a) V_O rich $SrTiO_3$ made with heating profile 1 and (b) V_O poor $SrTiO_3$ made with heating profile 2. Peaks that belong to rutile TiO_2 impurity are marked with asterisks (*) while peaks belonging to anatase TiO_2 impurity are marked with plus sign (+). ICSD 192314 was used for $SrTiO_3$.

Samples made with heating profile 1 contain the cubic $SrTiO_3$ ($\sim$95 wt%) as well as both rutile TiO_2 and anatase TiO_2 impurity which accounted for 5 wt% of the sample (Fig. 3). The impurity peaks of rutile and anatase TiO_2 were absent in the PXRD pattern of $SrTiO_3$ prepared *via* heating profile 2. We observed that the slower and longer heating profile 1 allowed the formation of TiO_2 impurities as opposed to the shorter and faster heating profile 2. As it was further determined by several characterization methods, the primary difference between $SrTiO_3$ samples produced *via* two heating profiles is the concentration of O vacancies: heating profile 1 resulted in the $SrTiO_3$ that is rich in O vacancies (V_O rich), while heating profile 2 leads to $SrTiO_3$ that is poor in O vacancies (V_O poor). For the sake of clarity, we refer to the samples prepared *via* heating profile 1 as "V_O rich" and *via* heating profile 2 as "V_O poor" throughout the text.

Since the doping of $SrTiO_3$ with aluminum has been reported to increase the rate of photocatalytic activity of $SrTiO_3$,[22–25] aluminum-doped samples $SrTi_{1-x}Al_xO_3$ were synthesized using the same two heating profiles. The maximum loading fraction of Al used was $x = 0.2$ because further increase in Al dopant concentration resulted in a $SrAlO_2$ impurity as evident from PXRD data. The doped samples made with heating profile 1 also have the anatase and rutile TiO_2 impurities. Similar to undoped $SrTiO_3$, these impurities are absent in the doped samples made with heating profile 2 because the faster and shorter heating profile does not favour the formation of TiO_2 impurities (Fig. 3). The replacement of Ti^{4+} (0.605 Å) in octahedral sites with smaller Al^{3+} (0.535 Å) is expected to result in the reduction of the cubic unit cell parameters. Rietveld refinement using LaB_6 as an internal standard was carried out to determine the change in unit cell upon Al doping (Fig. 4). The unit cell parameter of V_O rich $SrTi_{1-x}Al_xO_3$ are generally smaller than that V_O poor $SrTi_{1-x}Al_xO_3$ as shown in Fig. 4. As expected, with the increase of Al content, the unit cell parameter decreases until $x = 0.1$, *i.e.*, the unit cell parameter of $SrTi_{0.9}Al_{0.1}O_3$ is very similar to that of $SrTi_{0.8}Al_{0.2}O_3$, suggesting that maximal Al dopant concentration is $x < 0.2$.

The crystallite size of V_O rich samples calculated from the Debye Scherrer equation on average decreases with increase in aluminum doping while the crystallite size of V_O poor samples remain constant regardless of aluminum doping (Table 1).
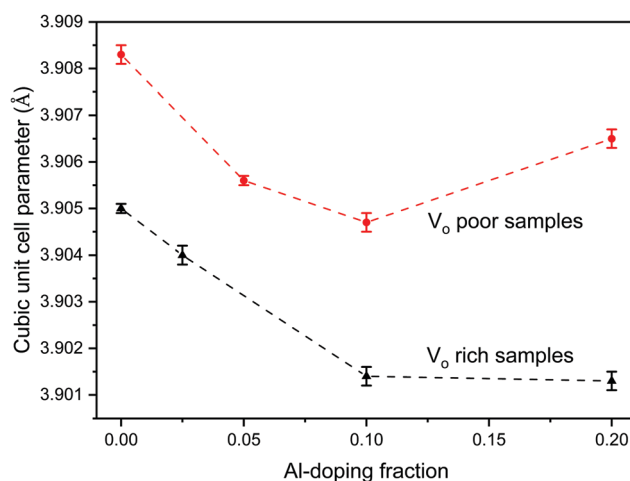

Fig. 4 Change in cubic unit cell parameter of the V_O rich $SrTi_{1-x}Al_xO_3$ made with heating profile 1 (black) and V_O poor $SrTi_{1-x}Al_xO_3$ made with heating profile 2 (red) as a function of Al doping, x.

Table 1 Crystallite sizes of the $SrTi_{1-x}Al_xO_3$ (x = 0 to 0.2)

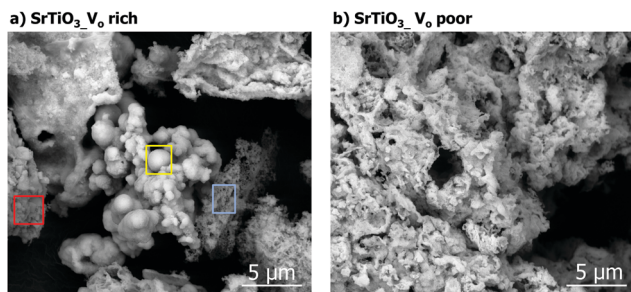| Samples	Crystallite size[a] (nm)	
	Heating 1 (V_O rich)	Heating 2 (V_O poor)
$SrTiO_3$	40 (6)	24(4)
$SrTi_{0.975}Al_{0.025}O_3$	31(5)	NA
$SrTi0.95Al0.05O_3$	27(2)	NA
$SrTi_{0.9}Al_{0.1}O_3$	26(4)	23(3)
$SrTi_{0.8}Al_{0.2}O_3$	21(3)	20(3)

[a] Calculated using Debye Scherrer equation.

Fig. 5 SEM image of (a) V_O rich $SrTiO_3$ made with heating profile 1 and (b) V_O poor $SrTiO_3$ made with heating profile 2.

Scanning electron microscopy (SEM) images of the samples showed the doped and undoped V_O rich $SrTiO_3$ have structured crystallites (in red, Fig. 5(a)), nanoclusters (in yellow, Fig. 5(a)), and flakes (in blue, Fig. 5(a)). On the contrary, the V_O poor samples all appeared to be in the form of flakes (or sheets), regardless of the presence or absence of aluminum (Fig. 5 and Fig. S1, ESI†). Energy Dispersive X-ray Spectroscopy (EDXS) of Al-doped sample indicates the homogeneous distribution of Sr, Ti and Al in the samples.

^{27}Al solid-state NMR spectroscopy

Aluminum is expected to replace titanium in the octahedral site of the $SrTiO_3$ perovskite structure based on the similarity of ionic radii. ^{27}Al solid-state NMR spectra of the doped samples were obtained to prove doping of aluminum in a symmetric octahedral site in the perovskite structure (Fig. 6). ^{27}Al is a spin-

5/2 quadrupolar nucleus with a natural abundance of 100% and a high sensitivity to the coordination environment and symmetry. We note that solid-state NMR spectroscopy has previously been used to extensively characterize $SrTiO_3$ and related perovskite materials.[46–49] The NMR spectra were fitted to three signals: a broad peak with an isotropic shift (δ_{iso}) of ca. 83 ppm corresponding to a tetrahedral site, a broad signal with δ_{iso} of 16 ppm corresponding to an octahedral site, and a narrow signal with δ_{iso} of 9 ppm that is assigned to the doped octahedral site of the perovskite structure. The broad tetrahedral and octahedral signals are characteristic of alumina,[50] and were assigned to an amorphous alumina impurity that could not be detected by PXRD.[49] The tail of the broad ^{27}Al NMR signals at lower chemical shifts is indicative of a distribution of quadrupolar couplings that is intrinsic to amorphous alumina.[50] The sharp signal at 9 ppm represents a ^{27}Al site with low quadrupolar broadening and must therefore correspond to a site of high spherical symmetry; this observation confirms the aluminum doping into the titanium octahedral site in $SrTiO_3$. To ensure quantitative excitation of the various ^{27}Al signals, a small tip angle pulse was used (see experimental).[39,40]

Fig. 6(a) compares the ^{27}Al solid-state NMR obtained with different Al doping levels. Note that the intensities are normalized with respect to the sharp ^{27}Al NMR signal at 9 ppm. It is evident that as the Al doping level increases the concentration of the alumina impurity also increases. Next, the spectra were deconvoluted and fit using the Czjzek distribution to model the distribution in quadrupolar couplings of the alumina impurity (Fig. S2, ESI†). The fraction of the octahedral doped ^{27}Al sites in perovskite structure (% doping, Table 2) was then estimated from the absolute integrals of the deconvoluted peaks.

Notably, the actual fraction of aluminum doped into the structure (actual x, Table 2) was lower than the nominal fraction. As the nominal doping fraction increases, so does the actual doping fraction (Fig. 6(b)). However, the percentage of aluminum being doped into the structure decreases as the aluminum doping fraction increases, suggesting that at higher nominal Al fraction more alumina is forming (Table 2).

Diffuse reflectance and bandgap measurement

The diffuse reflectance was measured for all samples and expressed as Tauc plots to calculate the direct band gap (Fig. 7). All the V_O rich samples showed an approximate direct
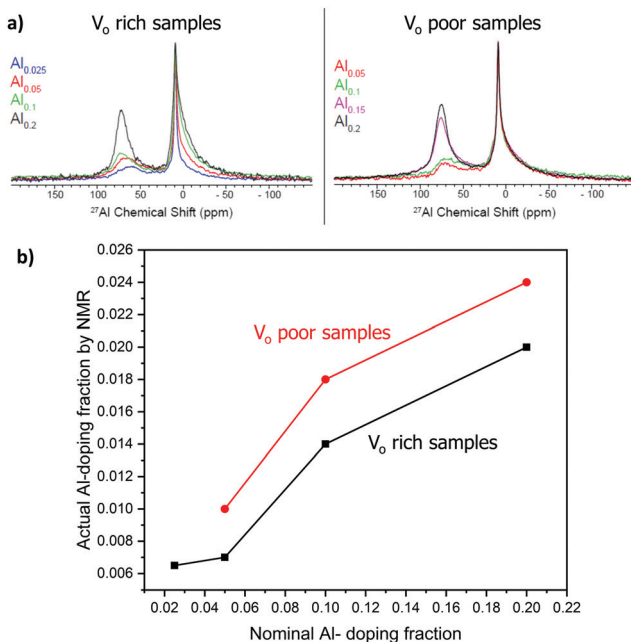

Fig. 6 ^{27}Al solid-state NMR. (a) Comparison of 1D spectra; signal intensities are normalized with respect the sharp signal at ca. 9 ppm. (b) Plot showing the actual and nominal aluminum doping concentration trend for V_O rich samples made with heating 1 (black curve) and V_O poor samples made heating 2 (red curve).

Table 2 Percent concentration of nominal aluminum actually doping into the structure

Nominal x in $SrTi_{1-x}Al_xO_3$	Heating 1 (V_O rich)		Heating 2 (V_O poor)	
	% Doping[a]	Actual x	% Doping[a]	Actual x
0.025	26	0.0065	NA	NA
0.05	14	0.007	20	0.01
0.1	14	0.014	18	0.018
0.2	10	0.02	12	0.024

[a] (Nominal x) × (% doping) = Actual x.

band gap of 3.0 eV and all V_O poor samples showed an approximate direct band gap of 3.2 eV as shown in Fig. 7 and Fig. S3 (ESI†). The doping of the samples with Al does not significantly affect their bandgaps for either heating profile. Doped and undoped $SrTiO_3$ samples made with heating profiles 1 and 2 showed beige colors but with different intensities. The color of the synthesized samples can be attributed to the presence of oxygen vacancies and high concentration of Ti^{3+}. It has been previously reported that $SrTiO_3$ samples containing a high amount of Ti^{3+} usually possess color,[22] in support of our observation.

Both undoped and doped samples made with heating profile 1 were darker beige in color, as shown in Fig. 7(a). A band tail (or an additional absorption edge) was also noticed in their absorption data (Fig. 7(c)). The darker beige color and a band tail suggest that samples made with heating profile 1 have more Ti^{3+} species and oxygen vacancies (V_O rich). This is in agreement with previous reports where the concentration of Ti^{3+}/oxygen vacancies in $SrTiO_3$ was increased by heating the sample in a reducing environment.[52,53] Similarly, the decomposition of the DES provides a reducing atmosphere during the synthesis which favors the formation of oxygen vacancies as it was previously shown for zinc and copper vanadates.[7,8]

Samples made with heating profile 2 (V_O poor) showed a lighter beige color and also a slightly wider bandgap (Fig. 7(b)). The absence of a pronounced band tail in the absorbance spectra of samples made with heating profile 2 (Fig. 7(c)) indicates a lower concentration of Ti^{3+} states.[51] Since the same color was observed in undoped sample and doped sample, we presume that the Al^{3+} dopant did not significantly suppress Ti^{3+} states.

X-Ray photoelectron spectroscopy

XPS measurements were carried out on the $SrTiO_3$ samples to quantify the amount of reduced Ti species. Fig. 8 shows Ti 2p core level spectra of $SrTiO_3$ made with both heating profiles. The two titanium peaks shown originate from spin–orbit splitting of Ti $2p_{3/2}$ and Ti $2p_{1/2}$, each peak is a superposition of 3 components corresponding to Ti^{4+}, Ti^{3+}, and Ti^{2+}. Fig. 8(a) shows the titanium species in V_O rich $SrTiO_3$. The doublet in red at 458.7 eV (Ti $2p_{3/2}$) and 464.4 eV (Ti $2p_{1/2}$) are assigned to Ti^{4+}, the doublet in blue at 457.6 eV (Ti $2p_{3/2}$) and 463.0 eV (Ti $2p_{1/2}$) are assigned to Ti^{3+}, while the doublet in magenta at 455.4 eV and 461.4 eV are assigned to Ti^{2+}. Based on the relative Ti $2p_{3/2}$ peak ratios, the V_O rich sample has 73.5% of titanium present as Ti^{3+}, 19.2% as Ti^{4+}, and 7.3% as Ti^{2+}. The large quantity of Ti^{3+} present in oxygen vacancy rich $SrTiO_3$ agrees with the optical properties as discussed above. Fig. 8(b) shows the titanium species in the V_O poor $SrTiO_3$. The doublet in red at 458.5 eV (Ti $2p_{3/2}$) and 464.2 eV (Ti $2p_{1/2}$) are assigned to Ti^{4+}, the doublet in blue at 457.1 eV (Ti $2p_{3/2}$) and 462.9 eV (Ti $2p_{1/2}$) are assigned to Ti^{3+}, while the doublet in magenta at 455.3 eV and 461.1 eV are assigned to Ti^{2+}. In contrast to the V_O rich sample, the V_O poor $SrTiO_3$ sample made with heating profile 2 has 72.5% of titanium present as Ti^{4+}, 20.8% as Ti^{3+} and 6.7% as Ti^{2+}. The values of the binding energy of the titanium species
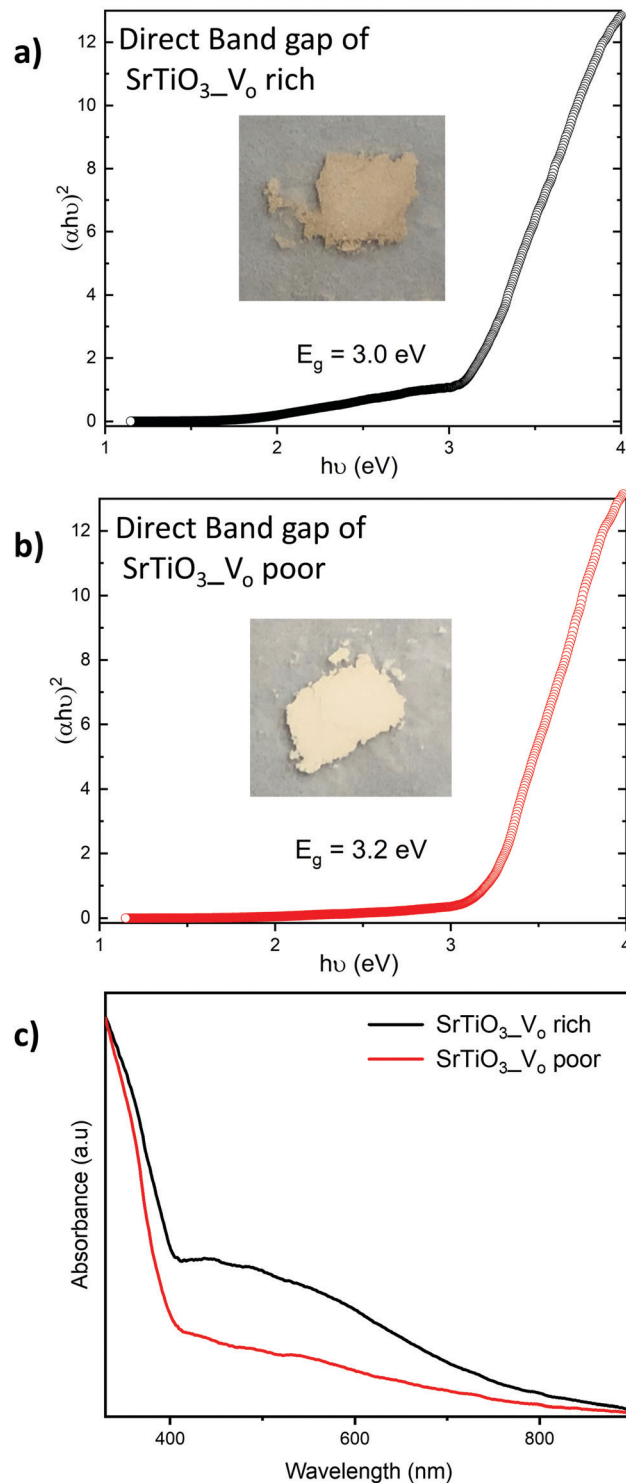

Fig. 7 Tauc plots used to determine direct band gaps of (a) V_O rich $SrTiO_3$ obtained *via* heating profile 1 and (b) Vo poor $SrTiO_3$ obtained *via* heating profile 2. Insets show the images of $SrTiO_3$ samples obtained *via* respective heating profiles. c) UV-Vis spectra of V_O rich $SrTiO_3$ obtained *via* heating profile 1 (black curve) and Vo poor $SrTiO_3$ obtained *via* heating profile 2 (red curve).

observed in this work are similar to those that have previously been reported.[22,54] The presence of Ti^{3+} and Ti^{2+} in the V_O rich
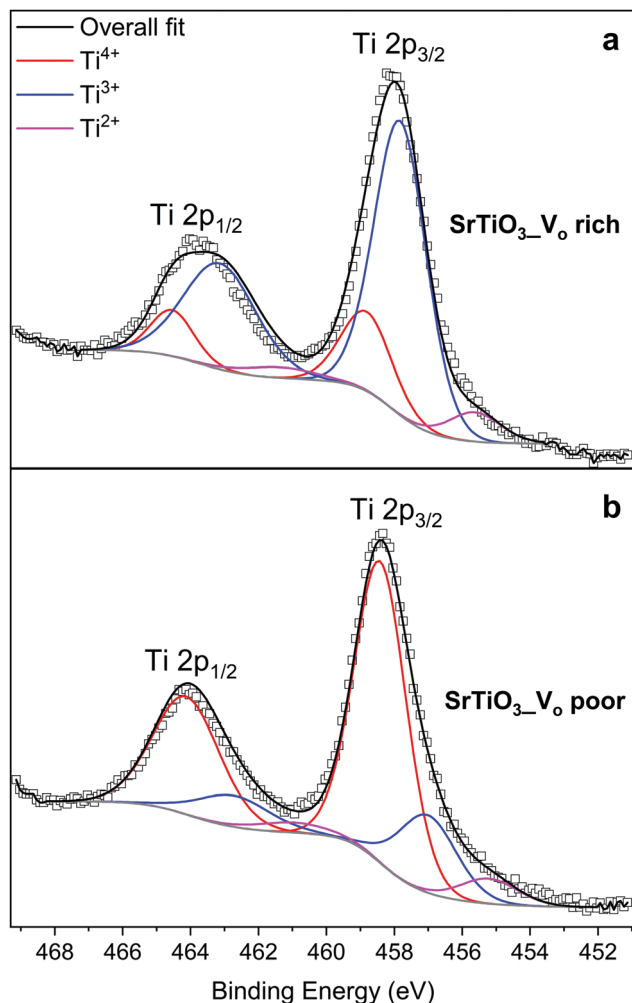
Fig. 8 XPS spectra of the Ti 2p region: (a) V_O rich $SrTiO_3$ made with heating profile 1 and (b) V_O poor $SrTiO_3$ made with heating profile 2.
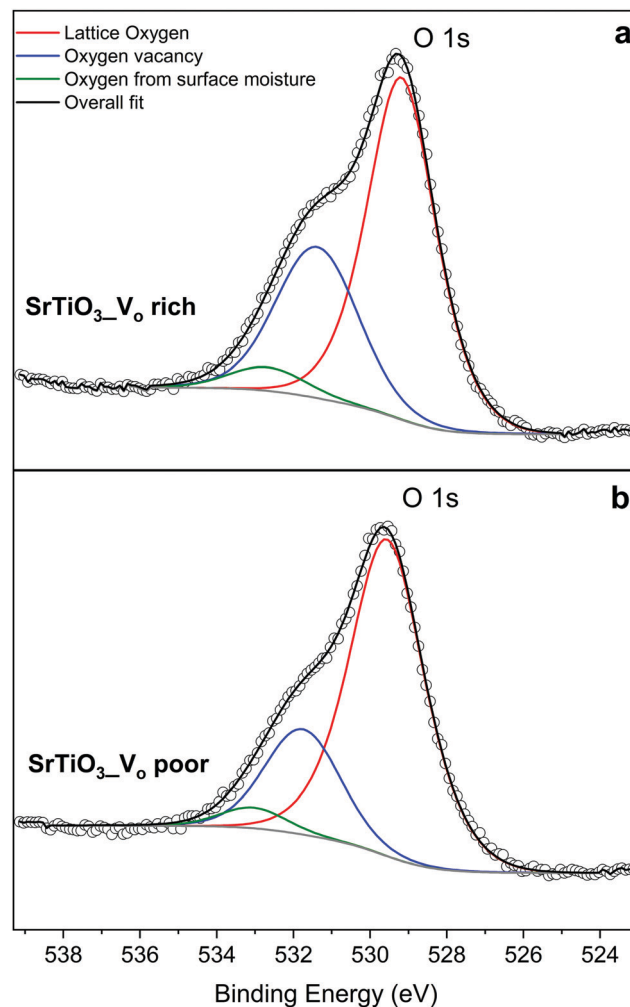

Fig. 9 XPS data of the oxygen species in (a) V_O rich $SrTiO_3$ made with heating profile 1 and (b) V_O poor $SrTiO_3$ made with heating profile 2.

and poor $SrTiO_3$ suggests that the malonic acid–choline chloride DES provides a reducing atmosphere during the calcination of doped or undoped $SrTiO_3$ samples. The prolonged heating of a sample in this reducing atmosphere leads to the increased amount of Ti^{3+} in the V_O rich samples made with heating profile 1. The XPS spectra in the Sr 3d region are similar for $SrTiO_3$ prepared by both heating methods, suggesting that Sr is in +2 oxidation state, irrespective of the heating profile used (Fig. S4, ESI†).

The O 1s spectra shown in Fig. 9 can also be fitted with 3 peaks. Fig. 9(a) represents the O 1s spectra of V_O rich $SrTiO_3$. The peak in red at 529.0 eV[22,52] corresponds to the lattice oxygen in the crystal structure of $SrTiO_3$, the blue peak at 531.2 eV[52] suggests the oxygen vacancies within the synthesized sample, and the green peak at 532.5[55] likely corresponds to loosely bound oxygen species at the sample due to atmospheric moisture. The O 1s spectra of V_O poor $SrTiO_3$ shown in Fig. 9(b) are shifted to higher binding energies by 0.6 eV. The fitted peak with the red line observed at 529.6 eV is attributed to the lattice oxygen, the fitted peak with the blue line at 531.8 eV corresponds to the oxygen vacancy and the fitted peak in green at

533.1 eV corresponds to the loosely bound oxygen from surface moisture. The amount of oxygen vacancy in the V_O rich $SrTiO_3$ sample was deduced from the fitted peaks in blue to be 32.4% while the V_O poor $SrTiO_3$ sample had 23.6% oxygen vacancy. The larger quantity of oxygen vacancies in V_O rich $SrTiO_3$ made with heating profile 1 can also explain its smaller unit cell parameter (Fig. 4). V_O rich $SrTiO_3$ has a unit cell parameter of 3.9050(4) Å which is 0.003 Å smaller than the unit cell parameter of V_O poor $SrTiO_3$. The same trend is seen for Al-doped $SrTiO_3$ prepared via two heating profiles with V_O rich Al-doped $SrTiO_3$ having overall smaller unit cell parameter compared to V_O poor Al-doped $SrTiO_3$ (Fig. 4). It should be noted that an atomic vacancy cannot be directly measured by the XPS, so the peaks assigned to the oxygen vacancy actually correspond to oxygen atoms near the vacant site. The survey spectra (Fig. S5, ESI†) suggest the absence of any other impurity element except the expected surface carbon, albeit the detection limit of XPS is 0.1–1 at%. It should also be noted that XPS is a surface technique and the percent of Ti^{3+}/oxygen vacancies is not representative of the bulk sample.

Photocatalytic activity

The photocatalytic activity of $SrTiO_3$ for overall water splitting under UV illumination was investigated after loading a $Rh_xCr_{2-x}O_3$ proton reduction cocatalyst (for details see experimental section). As can be seen from Fig. 10 and Fig. S6 (ESI†), all samples evolve only small amounts of H_2 and only trace amounts of O_2 can be detected, likely from residual dissolved oxygen in the reaction mixtures. This suggests that H_2 evolution is stoichiometric, not catalytic, and the $SrTiO_3$ samples themselves serve as the electron source for the evolved H_2. We find that V_O poor $SrTiO_3$ showed a higher H_2 evolution rate than that of the V_O rich $SrTiO_3$. This suggests that photocatalytic H_2 evolution activity and V_O/Ti^{3+} are inversely correlated. The H_2 amounts also varied with Al^{3+} content, although no activity
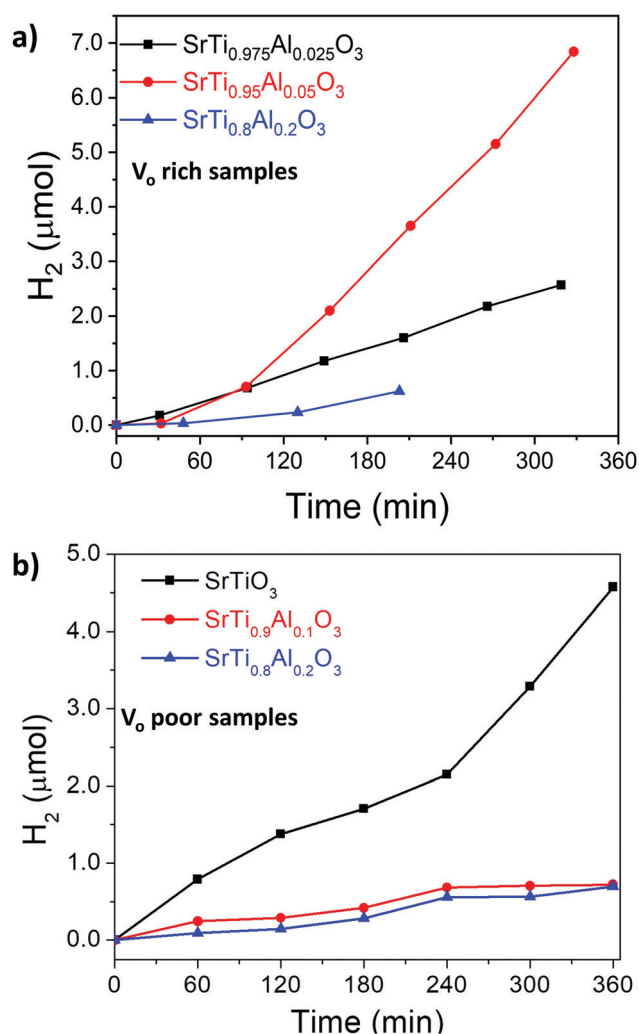

Fig. 10 Hydrogen evolution of (a) V_O rich samples made with heating profile 1 and (b) V_O poor samples made with heating profile 2 from water. Conditions: 100 mW cm^{-2} UV light from Xe-arc lamp, 100 mg $Rh_xCr_{2-x}O_3/SrTiO_3$ (or $Rh_xCr_{2-x}O_3/SrTiO_3$:Al) powder in 100 mL water. Oxygen was also detected for Vo rich samples made with heating 1 (see also Fig. S6, ESI†), while no oxygen was detected for Vo poor samples made with heating 2.
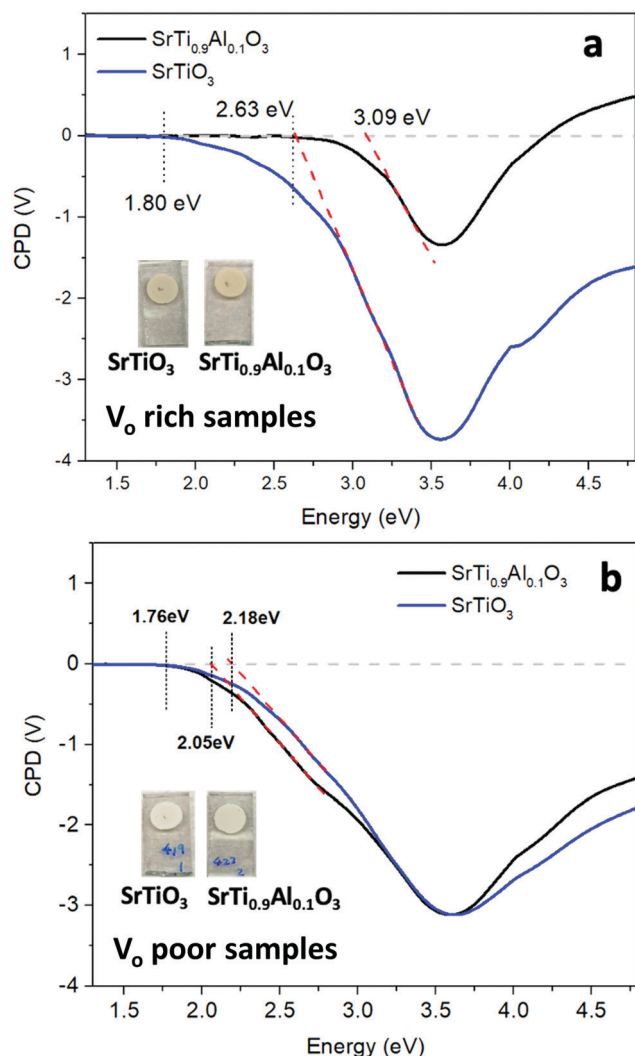
increase or trend could be seen. These findings are in contrast with previous observations of strong water splitting activity with micro- and nanosized Al-doped $SrTiO_3$ made by flux or hydrothermal syntheses.[22–25,56] Those samples had mostly cubic morphology and well-defined facets which promoted carrier separation. The necessity for a well-faceted highly crystalline photocatalyst was further emphasized in the recent work by Takata et al.[25] It was reported that oxygen evolution reaction preferably occurred on the (110) facets while hydrogen evolution reactions occurred on the (100) facets. As previously reported by Zhao et al.,[22] the Ti^{3+} sites act as recombination sites for photogenerated holes and electrons which leads to a reduction in the photocatalytic activity of $SrTiO_3$. We therefore hypothesize that the absence of water splitting activity in the DES-synthesized materials is a result of both the absence of a faceted morphology, as well as the presence of a substantial amount of Ti^{3+} recombination sites. This hypothesis is supported by separate H_2 evolution experiments on Pt-modified V_O rich $SrTiO_3$ and Al–$SrTiO_3$ samples in aqueous methanol (Fig. S7, ESI†). Again, only low H_2 amounts are formed with external quantum efficiencies (EQE) of 0.017% and 0.0121% (both at 375 nm) for Pt/$SrTiO_3$ and Pt/$SrTi_{0.9}Al_{0.1}O_3$, respectively. These reactions use methanol as an easy-to oxidize sacrificial electron donor and Pt as an efficient proton reduction co-catalyst. The low EQE values confirm that the low photocatalytic activity is intrinsic to the DES-synthesized materials.

To study the photochemical charge separation ability of V_O rich and poor $SrTiO_3$ and $SrTi_{0.9}Al_{0.1}O_3$, surface photovoltage (SPV) spectroscopy was conducted on particle films on FTO (Fig. 11). Here, a vibrating gold probe measures the contact potential difference (CPD) of the sample. The CPD value in the dark is given by the Fermi level difference between the gold probe and the sample, while the change (ΔCPD) under illumination equals the surface photovoltage.[57,58] The SPV spectrum for V_O rich Al^{3+}-doped $SrTiO_3$ in Fig. 11(a) shows an SPV onset at 2.63 eV and a maximum SPV signal at 3.6 eV. From the tangent of this major signal, the effective band gap of 3.09 eV can be extracted. This value is in good agreement with the optical bandgap in Fig. 7. Hence, the major photovoltage signal is attributed to band gap excitation of Al^{3+}-doped $SrTiO_3$ and charge transfer as shown in Fig. 12. The spectrum for the V_O rich Al^{3+}-free $SrTiO_3$ is also shown in Fig. 11(a). Here, the photovoltage signal starts at 1.8 eV and the effective bandgap appears at 2.63 eV. These low energy features are attributed to excitation of Ti^{3+} mid-gap states as shown in Fig. 12, and hole trapping in $SrTiO_3$ surface states. Based on the SPV spectroscopy data, the Ti^{3+} mid-gap state's concentration in V_O rich Al^{3+}-doped $SrTiO_3$ is greatly reduced. This confirms that Al^{3+} doping eliminates Ti^{3+} states for the V_O rich samples obtained via heating profile 1.

SPV spectra for the V_O poor samples are shown in Fig. 11(b). Again, the photovoltage maximum is seen at 3.6 eV, but this time the photovoltage onset and the effective band gaps of both samples occur much earlier (2.05–2.18 eV). This suggests that V_O poor undoped and Al-doped $SrTiO_3$ have higher mid-bandgap defect concentrations than V_O rich samples. Also, this

Fig. 11 Surface photovoltage (SPV) spectra of SrTiO$_3$ (blue) and SrTi$_{0.9}$Al$_{0.1}$O$_3$ (black) (a) V$_O$ rich made by heating profile 1 and (b) V$_O$ poor made by heating profile 2, respectively. CPD values under illumination are reported relative to the dark. The band-like onset was approximated by linear extrapolation (red dash). The inset pictures show the appearance of the respective films used for SPV measurement.

Fig. 12 Charge transfer and energetics during the SPV experiment for V$_O$ rich SrTiO$_3$ and Al-doped SrTiO$_3$ (heating 1). In SrTiO$_3$:Al, Ti^{3+} trap states were eliminated by Al^{3+} doping, leading to a less reducing Fermi level, fewer trapped electrons, and less band bending. The lower band bending in SrTiO$_3$:Al is indicated by the lesser surface photovoltage signal. $E_{Surface}$ denotes the energy of surface states resulting from dangling bonds, reduced ions, or surface adsorbates. Ti^{3+} and V$_O$ lattice defects (shown in red) are responsible for the sub-band gap photovoltage signal. E_{FTO} is the Fermi level of the fluorine doped tin oxide substrate.

Conclusions

SrTiO$_3$ and Al-doped SrTiO$_3$ were synthesized using a deep eutectic solvent consisting of a choline chloride and malonic acid mixture; the properties of the synthesized samples were investigated without any post-synthesis treatment. Titanium(IV) oxide bis(2,4-pentanedionate) employed in the synthesis as a titanium precursor is a stable powder which is easy to handle and dissolve in a choline chloride–malonic acid DES. ^{27}Al solid-state NMR showed that Al^{3+} was indeed doped into the symmetric octahedral Ti^{4+} site and also revealed the presence of an amorphous alumina impurity which was not detected by PXRD. The unit cell size, oxygen deficiency, Al-doping fraction and bandgap were tuned by variation in heating profile. Samples made with longer dwelling time and slower ramping (heating profile 1) had more of TiO$_2$ impurity and bigger crystallite sizes. Perovskite SrTiO$_3$ prepared via longer heating exhibits higher concentration of oxygen vacancies (V$_O$ rich) and Ti^{3+} species, resulting in darker beige color, smaller bandgap and a smaller unit cell size. Samples made with shorter dwelling times and faster ramping rate (heating profile 2) are characterized by higher purity and smaller crystallite sizes. Strontium titanate prepared via this method has lower concentration of Ti^{3+}/oxygen vacancies (V$_O$ poor), resulting in lighter beige color, wider band-gap, and larger cubic unit cell volume. Surface photovoltage spectroscopy confirms that Al^{3+} dopants can eliminate Ti^{3+} defects in Al-doped SrTiO$_3$ (heating 1), but that Al^{3+} doping has no effect on the defects in SrTiO$_3$ (heating 2). The latter defects might be a result of unintentional doping of trace amount of carbon, nitrogen or chlorine from the DES which are below the detection of X-ray photoelectron spectroscopy. The defects and the lack of clear facets are reasons for the lack of photocatalytic activity of the synthesized materials for water splitting or hydrogen evolution from aqueous methanol.

Conflicts of interest

There are no conflicts to declare.

time, Al^{3+} doping does not eliminate the sub-bandgap signal, suggesting that the defects are not from Ti^{3+}. This suggests that V$_O$ poor Al-doped and undoped SrTiO$_3$ contain additional impurities, likely at their surface. As shown in the SEM images (Fig. 5(a), (b) and Fig. S1a, b, ESI†), fast heating profile 2 produces V$_O$ poor SrTiO$_3$ with more irregular particle morphology, which may be correlated with structural defects or the unintentional doping of a minute amount of carbon, nitrogen or chlorine arising from trapping of volatiles or incomplete burn-off of the organic eutectic. It should be noted that SPV band gaps are often smaller than optical band gaps because SPV is more sensitive to states in the forbidden region near the band edges. Additionally, the sensitivity of SPV measurement to the impurity elements is higher than that of XPS.[59]
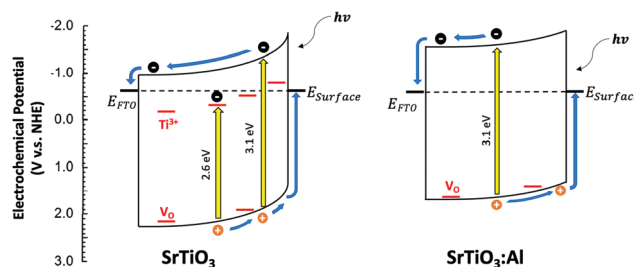
Acknowledgements

References

1 A. P. Abbott, G. Capper, D. L. Davies, R. K. Rasheed and V. Tambyrajah, *Chem. Commun.*, 2003, 70–71.

2 A. P. Abbott, D. Boothby, G. Capper, D. L. Davies and R. K. Rasheed, *J. Am. Chem. Soc.*, 2004, **126**, 9142–9147.

3 A. P. Abbott, G. Capper, D. L. Davies, K. J. McKenzie and S. U. Obi, *J. Chem. Eng. Data*, 2006, **51**, 1280–1282.

4 Q. H. Zhang, K. D. Vigier, S. Royer and F. Jerome, *Chem. Soc. Rev.*, 2012, **41**, 7108–7146.

5 X. Ge, C. D. Gu, X. L. Wang and J. P. Tu, *J. Mater. Chem. A*, 2017, **5**, 8209–8229.

6 A. Soldner, J. Zach, M. Iwanow, T. Gartner, M. Schlosser, A. Pfitzner and B. Konig, *Chem. – Eur. J.*, 2016, **22**, 13108–13113.

7 S. Hong, R. M. Doughty, F. E. Osterloh and J. V. Zaikina, *J. Mater. Chem. A*, 2019, **7**, 12303–12316.

8 S. Hong, S. J. Burkhow, R. M. Doughty, Y. Cheng, B. J. Ryan, A. Mantravadi, L. T. Roling, M. G. Panthani, F. E. Osterloh, E. A. Smith and J. V. Zaikina, *Chem. Mater.*, 2021, **33**(5), 1667–1682.

9 R. Boston, P. Y. Foeller, D. C. Sinclair and I. M. Reaney, *Inorg. Chem.*, 2017, **56**, 542–547.

10 R. C. Neville, C. A. Mead and B. Hoeneise, *J. Appl. Phys.*, 1972, **43**, 2124.

11 A. Tkach, O. Okhay, P. M. Vilarinho and A. L. Kholkin, *J. Phys.: Condens. Matter*, 2008, **20**, 415224.

12 J. Qi, M. Cao, J. P. Heath, J. S. Dean, H. Hao, Z. Yao, Z. Yu and H. Liu, *J. Mater. Chem. C*, 2018, **6**, 9130–9139.

13 J. B. Li, J. Wang, J. F. Li, Y. Li, H. Yang, H. Y. Yu, X. B. Ma, X. B. Yaer, L. Liu and L. Miao, *J. Mater. Chem. C*, 2018, **6**, 7594–7603.

14 A. I. Abutaha, S. R.-S. Kumar, A. M. Dehkordi, T. M. Tritt and H. N. Alshareef, *J. Mater. Chem. C*, 2014, **2**, 9712–9719.

15 K. van Benthem, C. Elsasser and R. H. French, *J. Appl. Phys.*, 2001, **90**, 6156–6164.

16 T. Tomio, H. Miki, H. Tabata, T. Kawai and S. Kawai, *J. Appl. Phys.*, 1994, **76**, 5886–5890.

17 B. L. Phoon, C. W. Lai, J. C. Juan, P.-L. Show and G.-T. Pan, *Int. J. Hydrogen Energy*, 2019, **44**, 14316–14340.

18 A. Frye, R. H. French and D. A. Bonnell, *Z. Metallkd.*, 2003, **94**, 226–232.

19 J. G. Mavroides, J. A. Kafalas and D. F. Kolesar, *Appl. Phys. Lett.*, 1976, **28**, 241–243.

20 K. Domen, S. Naito, M. Soma, T. Onishi and K. Tamaru, *J. Chem. Soc., Chem. Commun.*, 1980, 543–544.

21 T. Takata and K. Domen, *J. Phys. Chem. C*, 2009, **113**, 19386–19388.

22 Z. Q. Zhao, R. V. Goncalves, S. K. Barman, E. J. Willard, E. Byle, R. Perry, Z. K. Wu, M. N. Huda, A. J. Moule and F. E. Osterloh, *Energy Environ. Sci.*, 2019, **12**, 1385–1395.

23 Y. Ham, T. Hisatomi, Y. Goto, Y. Moriya, Y. Sakata, A. Yamakata, J. Kubota and K. Domen, *J. Mater. Chem. A*, 2016, **4**, 3027–3033.

24 Z. Q. Zhao, E. J. Willard, H. Li, Z. K. Wu, R. H.-R. Castro and F. E. Osterloh, *J. Mater. Chem. A*, 2018, **6**, 16170–16176.

25 T. Takata, J. Z. Jiang, Y. Sakata, M. Nakabayashi, N. Shibata, V. Nandal, K. Seki, T. Hisatomi and K. Domen, *Nature*, 2020, **581**, 411–414.

26 R. Konta, T. Ishii, H. Kato and A. Kudo, *J. Phys. Chem. B*, 2004, **108**, 8992–8995.

27 J. S. Wang, S. Yin, M. Komatsu, Q. W. Zhang, F. Saito and T. Sato, *Appl. Catal., B*, 2004, **52**, 11–21.

28 E. Rocha-Rangel, J. Lopez-Hernandez, J. A. Rodriguez-Garcia, E. N. Armendariz-Mireles, C. A. Calles-Arriaga, W. J. Pech-Rodriguez and J. A. Castillo-Robles, *J. Ceram. Process. Res.*, 2017, **18**, 590–593.

29 Y. Z. Fan, Z. Y. Zhou, Y. Chen, W. Huang and X. L. Dong, *J. Mater. Chem. C*, 2020, **8**, 50–57.

30 Y. Yamaguchi, Y. Kanamaru, M. Fukushima, K. Fujimoto and S. Ito, *J. Am. Ceram. Soc.*, 2015, **98**, 3054–3061.

31 Y. Ma, Z. J. Wu, H. W. Wang, G. Q. Wang, Y. K. Zhang, P. C. Hu, Y. M. Li, D. K. Gao, H. Q. Pu, B. Z. Wang and X. W. Qi, *CrystEngComm*, 2019, **21**, 3982–3992.

32 Z. R. Wang, X. C. Ren, C. W. Leung, S. Q. Shi and P. K.-L. Chan, *J. Mater. Chem. C*, 2013, **1**, 3825–3832.

33 G. Pfaff, *J. Mater. Chem.*, 1993, **3**, 721–724.

34 L. H. Hu, C. D. Wang, R. M. Kennedy, L. D. Marks and K. R. Poeppelmeier, *Inorg. Chem.*, 2015, **54**, 740–745.

35 L. A. Crosby, B. R. Chen, R. M. Kennedy, J. G. Wen, K. R. Poeppelmeier, M. J. Bedzyk and L. D. Marks, *Chem. Mater.*, 2018, **30**, 841–846.

36 T. K. Townsend, N. D. Browning and F. E. Osterloh, *ACS Nano*, 2012, **6**, 7420–7426.

37 *PDXL: Integrated X-ray powder diffraction software, Version 2.8.1.1*, Rigaku, 2018.

38 V. Petricek, M. Dusek and L. Palatinus, *Z. Kristallogr.*, 2014, **229**(5), 345–352.

39 A. Samoson and E. Lippmaa, *Phys. Rev. B: Condens. Matter Mater. Phys.*, 1983, **28**, 6567–6570.

40 E. Lippmaa, A. Samoson and M. Magi, *J. Am. Chem. Soc.*, 1986, **108**, 1730–1735.

41 J.-B. d'Espinose de la Caillerie, C. Fretigny and D. Massiot, *J. Magn. Reson.*, 2008, **192**, 244–251.

42 S. G.-J. van Meerten, W. M.-J. Franssen and A. P.-M. Kentgens, *J. Magn. Reson.*, 2019, **301**, 56–66.

43 R. M. Doughty, F. A. Chowdhury, Z. Mi and F. E. Osterloh, *J. Chem. Phys.*, 2020, **153**, 144707.

44 K. Maeda, K. Teramura, H. Masuda, T. Takata, N. Saito, Y. Inoue and K. Domen, *J. Phys. Chem. B*, 2006, **110**, 13107–13112.

45 F. Wang, Q. Xu, Z.-a Tan, D. Qian, Y. Ding, L. Li, S. Li and Y. Li, *Org. Electron.*, 2012, **13**, 2429–2435.

46 S. F. Dec, M. F. Davis, G. E. Maciel, C. E. Bronnimann, J. J. Fitzgerald and S. S. Han, *Inorg. Chem.*, 1993, **32**, 955–959.

47 A. Faucher, V. V. Terskikh, E. Ye, G. M. Bernard and R. E. Wasylishen, *J. Phys. Chem. A*, 2015, **119**, 11847–11861.

48 I. Bykov, M. Makarova, V. Trepakov, A. Dejneka, L. Yurchenko, A. Jaeger and L. Jastrabik, *Phys. Status Solidi B*, 2013, **250**, 821–824.

49 C. Gervais, D. Veautier, M. E. Smith, F. Babonneau, P. Belleville and C. Sanchez, *Solid State Nucl. Magn. Reson.*, 2004, **26**, 147–152.

50 L. Samain, A. Jaworski, M. Eden, D. M. Ladd, D. K. Seo, F. J. Garcia-Garcia and U. Haussermann, *J. Solid State Chem.*, 2014, **217**, 1–8.

51 C. V. Chandran, C. E.-A. Kirschhock, S. Radhakrishnan, F. Taulelle, J. A. Martens and E. Breynaert, *Chem. Soc. Rev.*, 2019, **48**, 134–156.

52 H. Q. Tan, Z. Zhao, W. B. Zhu, E. N. Coker, B. S. Li, M. Zheng, W. X. Yu, H. Y. Fan and Z. C. Sun, *ACS Appl. Mater. Interfaces*, 2014, **6**, 19184–19190.

53 W. L. Zhao, W. Zhao, G. L. Zhu, T. Q. Lin, F. F. Xu and F. Q. Huang, *CrystEngComm*, 2015, **17**, 7528–7534.

54 M. C. Biesinger, L. W.-M. Lau, A. R. Gerson and R. S.-C. Smart, *Appl. Surf. Sci.*, 2010, **257**, 887–898.

55 M. C. Biesinger, B. P. Payne, L. W.-M. Lau, A. Gerson and R. S.-C. Smart, *Surf. Interface Anal.*, 2009, **41**, 324–332.

56 M. Klusackova, R. Nebel, K. M. Macounova, M. Klementova and P. Krtil, *Electrochim. Acta*, 2019, **297**, 215–222.

57 T. Dittrich and S. Fengler, *Surface Photovoltage Analysis of Photoactive Materials*, World Scientific Publishing Europe Ltd., London, 2020, p. 287.

58 J. Zhao and F. E. Osterloh, *J. Phys. Chem. Lett.*, 2014, **5**, 782–786.

59 J. Lagowski, P. Edelman, A. M. Kontkiewicz, O. Milic, W. Henley, M. Dexter, L. Jastrzebski and A. M. Hoff, *Appl. Phys. Lett.*, 1993, **63**, 3043–3045.